The Astrophysical Journal, 617:384–398, 2004 December 10
© 2004. The American Astronomical Society. All rights reserved. Printed in U.S.A.

A SURVEY OF LARGE MOLECULES OF BIOLOGICAL INTEREST TOWARD SELECTED HIGH-MASS STAR-FORMING REGIONS

A. Remijan,[1,2,3] Y.-S. Shiao,[1] D. N. Friedel,[1] D. S. Meier,[1] and L. E. Snyder[1]

Received 2004 August 6; accepted 2004 August 20

ABSTRACT

We have surveyed the high-mass Galactic star-forming regions G19.61−0.23, G45.47+0.05, and W75N for interstellar methanol (CH_3OH), formic acid (HCOOH), acetic acid (CH_3COOH), methyl formate ($HCOOCH_3$), methyl cyanide (CH_3CN), and ethyl cyanide (CH_3CH_2CN) with the Berkeley-Illinois-Maryland Association Array. From our observations, we have detected two new sources of interstellar HCOOH toward the hot core regions G19.61−0.23 and W75N. We have also made the first detections of CH_3CH_2CN and $HCOOCH_3$ toward G19.61−0.23. The relative $HCOOH/HCOOCH_3$ abundance ratio toward G19.61−0.23 is 0.18, which is comparable to the abundance ratios found by Liu and colleagues toward Sgr B2(N-LMH), Orion, and W51 (∼0.10). We have made the first detection of $HCOOCH_3$ toward W75N. The relative $HCOOH/HCOOCH_3$ abundance ratio toward W75N is 0.26, which is more than twice as large as the abundance ratios found by Liu and colleagues. Furthermore, the hot core regions around W75N show a chemical differentiation between the O and N cores similar to what is seen toward the Orion Hot Core and Compact Ridge and W3(OH) and W3(H_2O). It is also apparent from our observations that the high-mass star-forming region G45.47+0.05 does not contain any compact hot molecular core (HMC), and as a consequence its chemistry may be similar to that of cold dark clouds. Finally, the formation of CH_3COOH appears to favor HMCs with well-mixed N and O, despite the fact that CH_3COOH does not contain a N atom. If proved to be true, this is an important constraint on CH_3COOH formation and possibly other structurally similar biomolecules.

Subject headings: ISM: abundances — ISM: individual (G19.61−0.23, G45.47+0.05, W75N) — ISM: molecules

1. INTRODUCTION

Recently, there has been great interest in searching a variety of star-forming regions (SFRs) for biologically interesting molecules (biomolecules), including formic acid (HCOOH) and acetic acid (CH_3COOH), because they share common structural elements with glycine (NH_2CH_2COOH), the simplest amino acid (Remijan et al. 2003; Liu et al. 2001, 2002). By measuring the abundance and distribution of these structurally similar species, we are helping to constrain the number of sources that may contain interstellar glycine. Furthermore, large molecules such as CH_3COOH and methyl formate ($HCOOCH_3$) may provide important clues to the formation chemistry of large biomolecules. CH_3COOH, $HCOOCH_3$, and glycolaldehyde (CH_2OHCHO) are all isomers. However, $HCOOCH_3$ and CH_3COOH are detectable in the high-mass SFRs W51e2, G34.3+0.24, and Sgr B2(N-LMH) and show a very compact (∼2–10 arcsec^2) distribution, while CH_2OHCHO has only been detected toward Sgr B2(N-LMH) and shows a distribution extended over 1′ (Hollis et al. 2001). The different distributions demonstrate that these isomers form in different ways. The question remains as to why CH_3COOH and $HCOOCH_3$ have such a different distribution compared to CH_2OHCHO despite their identical atoms and atomic composition. By further investigating the sources where large biomolecules may be found, a better understanding of the chemistry under which these species are formed can be achieved.

There have been a number of molecular line surveys using single-element radio telescopes over the last several years that have detected many large molecules in various SFRs (see, e.g., Nummelin et al. 2000; Ikeda et al. 2001; Gibb et al. 2000; Hatchell et al. 1998; Helmich & van Dishoeck 1997; Helmich et al. 1994). However, to date, the only interferometric detections of HCOOH and CH_3COOH have been toward high-mass (>10 $M_\odot$) SFRs (Remijan et al. 2002, 2003; Liu et al. 2001). Two features that identify regions of high-mass star formation are ultracompact (UC) H II regions and H_2O masers. Dense regions of hot molecular gas are often associated with these regions, and these ''hot molecular cores'' (HMCs) have typical molecular hydrogen densities of $n \sim 10^5$–10^7 cm^{-3} and temperatures of 100–200 K. It is toward these regions in and surrounding HMCs that the bulk of large biomolecules are found. Therefore, to extend our database of sources that contain large biomolecules, we carried out observations toward three high-mass SFRs with the Berkeley-Illinois-Maryland Association (BIMA) Array.[4] Because arrays typically have better angular resolution than single-element radio telescopes and have larger fields of view, they are more suitable for determining the detailed distributions of the various molecular emissions, including the sizes and positions of compact emission sources. For species with compact distributions, this property will also lead to higher intensity lines and larger beam-averaged column densities.

Remijan et al. (2003) carried out an extensive survey of CH_3COOH toward both high-mass and low-mass SFRs. As a result of their survey, they detected a new source of interstellar

[1] Department of Astronomy, University of Illinois, Urbana, IL 61801; aremijan@astro.uiuc.edu, shaw2@astro.uiuc.edu, friedel@astro.uiuc.edu, meierd@astro.uiuc.edu, snyder@astro.uiuc.edu.

[2] Current address: NASA Goddard Space Flight Center, Earth and Space Data Computing Division, Code 930, Greenbelt, MD 20771.

[3] National Research Council Resident Research Associate.

[4] Operated by the University of California, Berkeley, the University of Illinois, and the University of Maryland with support from the National Science Foundation.

TABLE 1
COMBINED MAP PARAMETERS

Source (1)	Gain Calibrator (2)	Beam (arcsec × arcsec) (3)	Frequency (GHz) (4)	Channel rms[a] (Jy beam^{-1}) (5)
G19.61−0.23.....	1733−130	4.5 × 1.9	111.5	0.05
		16.9 × 5.4	110.3	0.60
G45.47+0.05	1925+211	3.3 × 1.9	111.5	0.04
		9.3 × 5.8	110.3	0.10
W75N [b]	2025+337	2.7 × 2.2	110.3	0.07
	2013+370	4.4 × 3.7	111.5	0.06

[a] The stated channel rms is given for the window containing the transitions of AcA at 111.5 GHz or the CH_3CN transitions at 110.3 GHz.
[b] Data toward W75N at 110.3 GHz used with permission from C. Watson (2003 Oct 16).

CH_3COOH toward the high-mass HMC G34.3+0.2. Furthermore, that survey suggested HMCs that have a mass range between 200 and 2000 $M_\odot$ and do not show differentiation between O and N chemistries are sources of interstellar CH_3COOH. In addition, the three known CH_3COOH sources are within 7 kpc of the Galactic center. Therefore, it appears galactocentric distance could be a factor in the abundance of CH_3COOH. Finally, Remijan et al. (2004) found that methyl cyanide (CH_3CN) is a better tracer of the large molecules ethyl cyanide (CH_3CH_2CN) and CH_3COOH than is $HCOOCH_3$ toward the HMCs W51 e1 and e2. In order to investigate these hypotheses, we observed CH_3CN, CH_3CH_2CN, methanol (CH_3OH), HCOOH, CH_3COOH, and $HCOOCH_3$ toward a sample of massive SFRs selected based on the above criteria.

2. OBSERVATIONS

The large molecule survey took place from 1999 October to 2003 November utilizing the B and C configurations of the BIMA Array. The minimum baseline for these observations was ∼8 m, and the maximum baseline was ∼150 m, providing angular resolutions of ∼2″–13″. Table 1 lists the parameters of the combined data sets of our survey.[5] To include all the data from a source with multiple tracks or in multiple arrays, the data were inverted in *u-v* space. The resulting synthesized beam size was determined by the region of heaviest *u-v* coverage. Column (1) lists the sources observed. Column (2) lists the sources used to calibrate the antenna-based gains. Saturn and Uranus were used as the flux density calibrators for these observations. The absolute amplitude calibration of these sources is accurate to within ∼20%. Column (3) lists the corresponding beam size, column (4) lists the rest frequency of each observation, and column (5) lists the approximate 1 σ channel rms noise level in the CH_3COOH or CH_3CN windows of the combined data sets. The passbands were calibrated automatically during data acquisition.[6] In the past, this method has been quite satisfactory and has not generated spurious features. In § 2.1 we describe the sources included in our large biomolecule survey.

Table 2 lists the molecular parameters of all the 41 observed transitions in our survey. Column (1) lists the species; column (2) lists the transition. Column (3) lists the calculated rest frequency and its 2 σ standard deviation. Column (4) lists the product of the line strength and the square of the relevant dipole moment; column (5) lists the upper state energy level of each transition. The estimated rotational partition functions are given in the footnotes. Each correlator configuration included the full *K* structure of CH_3CN, the two strongest ($10_{*,10}$–$9_{*,9}$ A and E) CH_3COOH transitions near 111.5 GHz, a HCOOH transition at 108 GHz, and several strong transitions of $HCOOCH_3$ and CH_3CH_2CN. The spectral windows containing these transitions had a bandwidth of 50 MHz and were divided into 128 channels for a spectral resolution of 0.39 MHz per channel. All data were combined, imaged, and self-calibrated using the MIRIAD software package (Sault et al. 1995). The 1 σ rms noise level of the final maps was used to set upper limits to the column densities of the undetected molecular species searched for in our survey.

2.1. *Sources*

Table 3 lists the three sources surveyed for CH_3CN, CH_3CH_2CN, CH_3OH, HCOOH, CH_3COOH, and $HCOOCH_3$ in column (1). Columns (2) and (3) list the pointing center for each observation. Columns (4) and (5) list the distance to each source from the Sun and from the Galactic center (galactocentric),[7] respectively. Finally, column (6) lists the mass of each SFR, and column (7) lists the systemic local standard of rest velocity (v_{LSR}). Each source was selected based on the conclusions of Remijan et al. (2003) that regions containing detectable amounts of the large biomolecule CH_3COOH are HMCs (1) between 200 and 2000 $M_\odot$, (2) within 7 kpc of the Galactic center, and (3) that are not known to show chemical differentiation between O and N chemistry. We discuss each source in detail below.

2.1.1. *G19.61−0.23*

G19.61−0.23 ($\alpha = 18^h27^m38\overset{s}{.}1$, $\delta = -11°56'39''$ [J2000.0]) is a well-studied high-mass SFR. Some of the earliest observations of G19.61−0.23 were performed by Matthews et al. (1977) as they identified radio continuum emission toward regions containing OH maser sources. They interpreted the large amount of extended structure as containing several H II regions. This region has been extensively studied for OH masers (Garay et al. 1985; Forster & Caswell 1989), H_2O masers (Forster &

[5] For a complete description of the observations taken between 1999 October and 2000 April toward W75N, see Watson et al. (2002).
[6] A technical description of this can be found at http://astron.berkeley.edu/~plambeck/technical.html.
[7] For a description of how galactocentric distance was determined, see Remijan et al. (2003).

TABLE 2
MOLECULAR LINE PARAMETERS

Species (1)	Transition (2)	Frequency[a] (MHz) (3)	$\langle S_{i,j}\mu^2 \rangle$ (debye^2) (4)	E_u (K) (5)
CH_3CN[b]	6(5)–5(5)	110,329.608 ± 120	28.1	196.3
	6(4)–5(4)	110,349.760 ± 200	51.0	132.3
	6(3)–5(3)	110,364.470 ± 100	68.9	82.6
	6(2)–5(2)	110,374.986 ± 120	81.6	47.0
	6(1)–5(1)	110,381.376 ± 120	89.3	25.7
	6(0)–5(0)	110,383.494 ± 120	91.9	18.6
$CH_3^{13}CN$[b]	6(3)–5(3)	110,309.847 ± 10	68.9	83.0
	6(2)–5(2)	110,320.438 ± 10	81.6	47.2
	6(1)–5(1)	110,326.795 ± 10	89.3	25.7
	6(0)–5(0)	110,328.914 ± 10	91.9	18.5
CH_3OH[c]	3(1)–4(0) A^+	107,013.850 ± 100	3.0	28.4
	15(−2)–15(1) E2	107,159.790 ± 100	2.6	305.0
CH_3OD[d]	3(1)–3(0) E1	110,475.760 ± 1826	3.8	22.2
	4(1)–4(0) E1	110,950.750 ± 2382	5.1	30.8
CH_3COOH[e]	$10_{*,10}$–$9_{*,9}$ E	111,507.270 ± 40	54.8	30.5
	$10_{*,10}$–$9_{*,9}$ A	111,548.533 ± 40	54.8	30.5
CH_3CH_2CN[f]	$17_{2,16}$–$17_{1,17}$	107,481.468 ± 46	91.5	70.0
	$12_{7,6}$–$11_{7,5}$	107,485.178 ± 26	117.3	88.1
	$12_{7,5}$–$11_{7,4}$	107,485.178 ± 26	117.3	88.1
	$12_{6,7}$–$11_{6,6}$	107,486.961 ± 26	133.4	73.6
	$12_{6,6}$–$11_{6,5}$	107,486.962 ± 26	133.4	73.6
	$12_{8,5}$–$11_{8,4}$	107,491.573 ± 28	98.8	104.7
	$12_{8,4}$–$11_{8,3}$	107,491.573 ± 28	98.8	104.7
	$12_{5,8}$–$11_{5,7}$	107,502.426 ± 26	147.0	61.4
	$12_{5,7}$–$11_{5,6}$	107,502.474 ± 26	147.0	61.4
	$12_{4,9}$–$11_{4,8}$	107,543.926 ± 26	158.1	51.4
	$12_{4,8}$–$11_{4,7}$	107,547.601 ± 26	158.1	51.4
	$12_{3,10}$–$11_{3,9}$	107,594.049 ± 28	166.8	43.6
HCOOH[g]	$5_{1,5}$–$4_{1,4}$	108,126.710 ± 160	9.3	18.8
$HCOOCH_3$[h]	$9_{2,8}$–$8_{2,7}$ E	107,537.189 ± 24	22.8	28.8
	$9_{2,8}$–$8_{2,7}$ A	107,543.746 ± 26	22.8	28.8
	$9_{8,2}$–$8_{8,1}$ A	110,455.358 ± 30	69.1	5.1
	$9_{8,1}$–$8_{8,0}$ A	110,455.358 ± 30	69.1	5.1
	$9_{8,2}$–$8_{8,1}$ E	110,457.971 ± 28	69.1	5.1
	$9_{7,2}$–$8_{7,1}$ E	110,525.598 ± 32	59.2	9.6
	$9_{7,3}$–$8_{7,2}$ A	110,535.182 ± 28	59.2	9.6
	$9_{7,2}$–$8_{7,1}$ A	110,535.184 ± 28	59.2	9.6
	$9_{7,3}$–$8_{7,2}$ E	110,535.955 ± 26	59.2	9.6
	$7_{2,6}$–$6_{1,5}$ E	110,550.217 ± 28	1.4	19.0
	$7_{2,6}$–$6_{1,5}$ A	110,560.053 ± 30	1.4	19.0
	$9_{4,5}$–$8_{4,4}$ A	111,453.327 ± 24	19.4	37.3

[a] Errors are 2 σ.
[b] Boucher et al. (1980); $Q_{\rm rot} = 0.98T_{\rm rot}^{3/2}$.
[c] Xu & Lovas (1997); $Q_{\rm rot} = 1.23T_{\rm rot}^{3/2}$.
[d] Anderson et al. (1988); $Q_{\rm rot} = 0.71T_{\rm rot}^{3/2}$.
[e] Ilyushin et al. (2001); $Q_{\rm rot} = 14.10T_{\rm rot}^{3/2}$.
[f] Lovas (1982); $Q_{\rm rot} = 7.17T_{\rm rot}^{3/2}$.
[g] Willemot et al. (1980); $Q_{\rm rot} = 1.71T_{\rm rot}^{3/2}$.
[h] Oesterling et al. (1999); $Q_{\rm rot} = 12.45T_{\rm rot}^{3/2}$.

Caswell 1989; Comoretto et al. 1990; Hofner & Churchwell 1996), and CH_3OH masers (Kalenskii et al. 1994; Larionov et al. 1999). Recently, one of the most extensive studies of the structure and molecular environments of the G19.61−0.23 region was performed by Garay et al. (1998). Using high-resolution (2″–3″) Very Large Array[8] observations, they mapped the ionized gas of this region using the H66α recombination line and the 1.6 GHz continuum, as well as the molecular gas using the (2, 2) inversion transition of NH_3. The ionized gas observations indicated at least five distinct H II regions, implying the presence of an OB association. The NH_3 observations showed molecular emission from three distinct clumps, one of which lies very near the center of the cluster of H II regions (Garay et al. 1998). Since these observations, the G19.61−0.23 region has been observed in other molecular species such as CS (Shirley et al. 2003; Wu & Evans 2003; Larionov et al. 1999), HCN (Wu & Evans 2003), and CO (Hofner et al. 2000). However, the largest molecular species observed toward this region is methyl acetylene (CH_3C_2H; Fontani

[8] The VLA is operated by the National Radio Astronomy Observatory, which is a facility of the National Science Foundation, operated under cooperative agreement by Associated Universities, Inc.

TABLE 3

HOT CORES AND THEIR PHYSICAL PARAMETERS

Source Name (1)	R.A. (J2000.0) (2)	Decl. (J2000.0) (3)	Distance (kpc) (4)	Galactocentric[a] (kpc) (5)	Mass ($M_\odot$) (6)	v_{LSR} (km s^{-1}) (7)
G19.61−0.23[b]	18 27 38.1	−11 56 39	3.5	4.8	450	40
G45.47+0.05[b]	19 14 25.6	11 09 26	8.3	6.3	250	62
W75N	20 38 36.6	42 37 32	2.0[c]	8.0	∼440[d]	10

NOTE.—Units of right ascension are hours, minutes, and seconds, and units of declination are degrees, arcminutes, and arcseconds.

[a] Galactocentric distance was determined using the procedure outlined in Remijan et al. (2003).

[b] Kurtz et al. (2000).

[c] Hunter et al. (1994).

[d] Watson et al. (2002).

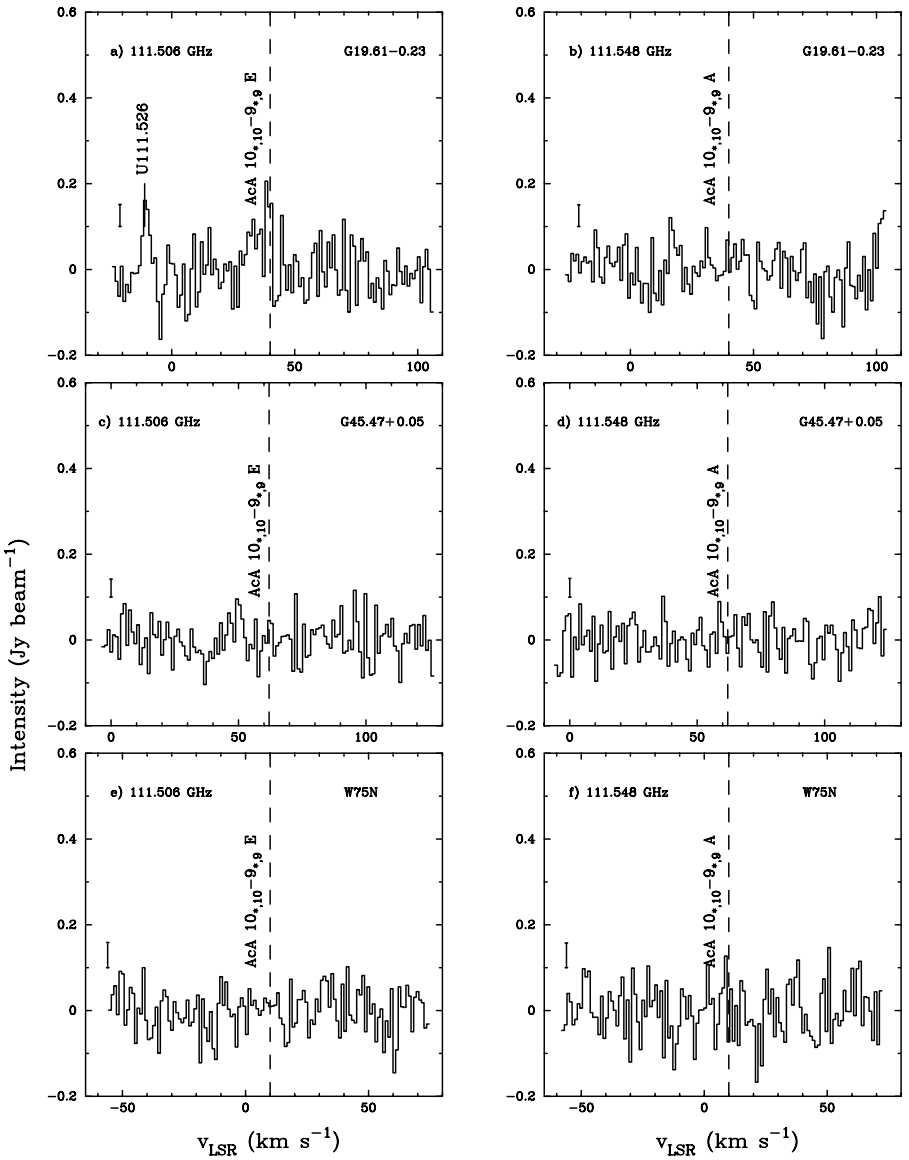

FIG. 1.—(*a*, *b*) Acetic acid (CH_3COOH, marked AcA) survey lines toward G19.61−0.23. The noise level is ∼60 mJy beam^{-1} (indicated by the vertical bar at the left of each panel). The spectral line labels correspond to the rest frequency located at the top left of each panel for a v_{LSR} of 40 km s^{-1} (*dashed line*). (*c*, *d*) Same as (*a*, *b*) except toward G45.47+0.05; rms ∼40 mJy beam^{-1}; v_{LSR} = 62 km s^{-1}. (*e*, *f*) Same as (*a*, *b*) except toward W75N; rms ∼50 mJy beam^{-1}; v_{LSR} = 10 km s^{-1}.

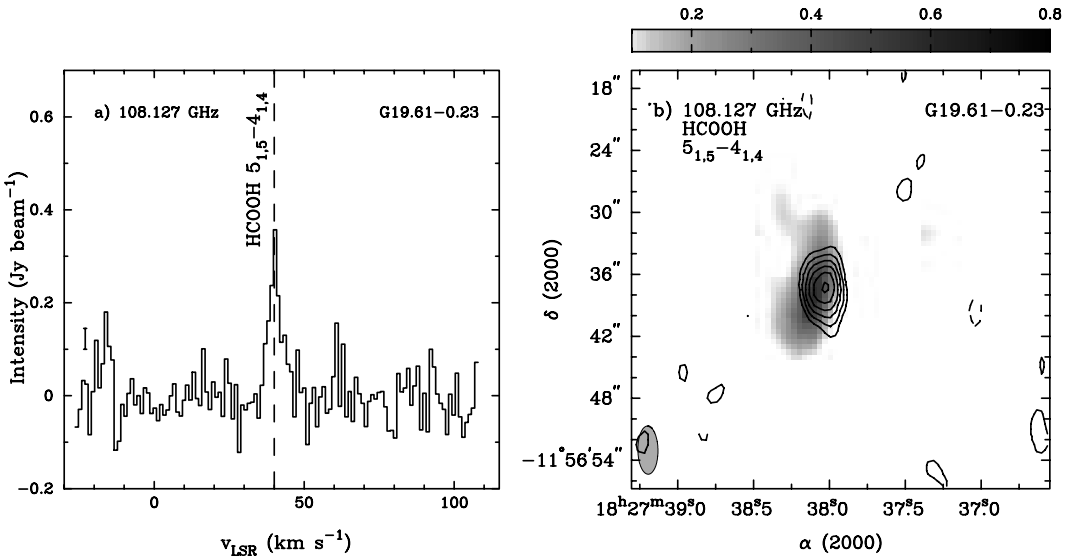

FIG. 2.—(*a*) HCOOH spectrum toward G19.61−0.23. The noise level is ∼40 mJy beam^{-1} (indicated by the vertical bar at the left of the spectrum). The spectral line label corresponds to the rest frequency located at the top left of the panel for a v_{LSR} of 40 km s^{-1} (*dashed line*). (*b*) Emission contours from the $5_{1,5}-4_{1,4}$ transition of HCOOH at 108.127 GHz overlaid on the G19.61−0.23 continuum emission at 108.1 GHz (*gray scale*). The numbers on the gray scale wedge are in units of Jy beam^{-1}. Contours indicate the location of the HCOOH emission near its peak at 40 km s^{-1}. The contour levels are −0.10, 0.10, 0.15, 0.20, 0.25, 0.30, and 0.35 Jy beam^{-1}. The synthesized beam of $5''.5 \times 2''.9$ is indicated at the bottom left corner.

et al. 2002) with the IRAM 30 m and FCRAO 14 m radio telescopes. Using an angular size of 30″ measured by Hofner et al. (2000) from $C^{17}O$ emission, Fontani et al. (2002) measured a rotational temperature of $T_{rot} = 56 \pm 7$ K and a total CH_3C_2H source-averaged column density of $N_{tot} = (1.1 \pm 3) \times 10^{15}$ cm^{-2}. They concluded from the rotation temperature diagram of the G19.61−0.23 region that the molecular gas was very close to LTE, and thus the measured rotational temperature is a good estimate of the kinetic temperature of the molecular gas. However, this region has never been surveyed at high resolution for large nitrogen-bearing species such as CH_3CH_2CN or oxygen-bearing molecules such as $HCOOCH_3$ and CH_3COOH. Therefore, our observations not only further constrain the detectability of CH_3COOH toward high-mass HMCs but also obtain information on the N and O chemistry present toward G19.61−0.23.

2.1.2. *G45.47+0.05*

G45.47+0.05 ($\alpha = 19^h14^m25^s.6$, $\delta = 11°09'26''$ [J2000.0]) is a high-mass SFR that has been extensively studied for OH masers (Matthews et al. 1977; Forster & Caswell 1989), H_2O masers (Forster & Caswell 1989; Churchwell et al. 1990), and CH_3OH masers (Zheng & Ling 1997; Larionov et al. 1999). Churchwell et al. (1992) searched this region for emission from CS, ^{13}CO, and CH_3CN. Using an excitation temperature of 100 K, they derived a total ^{13}CO column density of $N_{tot} = 3.6 \times 10^{17}$ cm^{-2} and a CS column density of $N_{tot} = 1.3 \times 10^{13}$ cm^{-2}. Initially, CH_3CN was not detected in this region. However, Olmi et al. (1993) conducted a survey of NH_3 and CH_3CN using the IRAM 30 m radio telescope. From their observations, they were able to construct rotational temperature diagrams (RTDs) and measured an approximate kinetic temperature of $T_k = 44 \pm 1$ K and a total CH_3CN beam-averaged column density of $N_{tot} = (2.5 \pm 5) \times 10^{13}$ cm^{-2}. For NH_3, they measured a rotational temperature of $T_{rot} = 39$ K and a total NH_3 beam-averaged column density of $N_{tot} = 4.4 \times 10^{14}$ cm^{-2}. One of the most extensive molecular line surveys done toward this source was performed by Hatchell et al. (1998) using the James Clerk Maxwell Radio Telescope. Their survey included lines of $C^{17}O$, SO, SO_2, CH_3OH, $^{13}CH_3OH$, CH_3CCH, CH_3CN, CH_3CH_2CN, CH_3OCH_3, $HCOOCH_3$, HC_3N, OCS, and CCH. From their survey, they detected lines of CH_3CN, CH_3C_2H, CH_3OH, $C^{17}O$, CO, and CCH and possibly $HCOOCH_3$ and HC_3N. However, they concluded from their survey that the hot core region toward G45.47+0.05 must be very small (<1″) or low in density (<10^8 cm^{-3}). Most recently, Fontani et al. (2002) observed transitions of CH_3C_2H and measured a source size of 35″ ± 8″ and from that, a rotational temperature of $T_{rot} = 39 \pm 7$ K and a total source-averaged CH_3C_2H column density of $N_{tot} = (5.0 \pm 3) \times 10^{14}$ cm^{-2}. Our observations investigated this region at high resolution (<10 arcsec^2) for large, biologically interesting molecules including HCOOH and CH_3COOH, in an attempt to detect any molecular emission associated with a compact HMC.

2.1.3. *W75N*

W75N ($\alpha = 20^h38^m36^s.6$, $\delta = 42°37'32''$ [J2000.0]) is a massive SFR containing several UC H II regions that has been a target of many surveys since its detection by Westerhout (1958). Primarily, this region has been extensively studied for OH masers (e.g., Palmer et al. 2003, 2004; Gasiprong et al. 2002), H_2O masers (e.g., Valdetto et al. 2002; Lekht & Krasnov 2000; Torelles et al. 1997), CH_3OH masers (Voronkov et al. 2002; Lekht et al. 2002; Minier et al. 2001), and H_2CO masers (Mehringer et al. 1995). There have been very few surveys of this source for large molecules. The most recent was performed by Kalenskii et al. (2002). In that survey, they searched for thermal CH_3OH lines as well as lines of CH_3CN, HC_3N, $HCOOCH_3$, and SO_2 with the IRAM 30 m radio telescope. They successfully detected the CH_3OH transitions but no emission from any of the other molecular species. However, Pankonin et al. (2001) successfully detected emission from CH_3CN using the Heinrich Hertz Telescope. From their observations, they measured a rotational temperature $T_{rot} = 135 \pm 33$ K and a total CH_3CN beam-averaged column density of $N_{tot} = (2.3 \pm 3) \times 10^{14}$ cm^{-2} within the 35″ beam. More recently, Watson et al. (2002) followed up the observations of Pankonin et al. (2001) toward W75N using the BIMA Array. They concluded that the CH_3CN emission coming

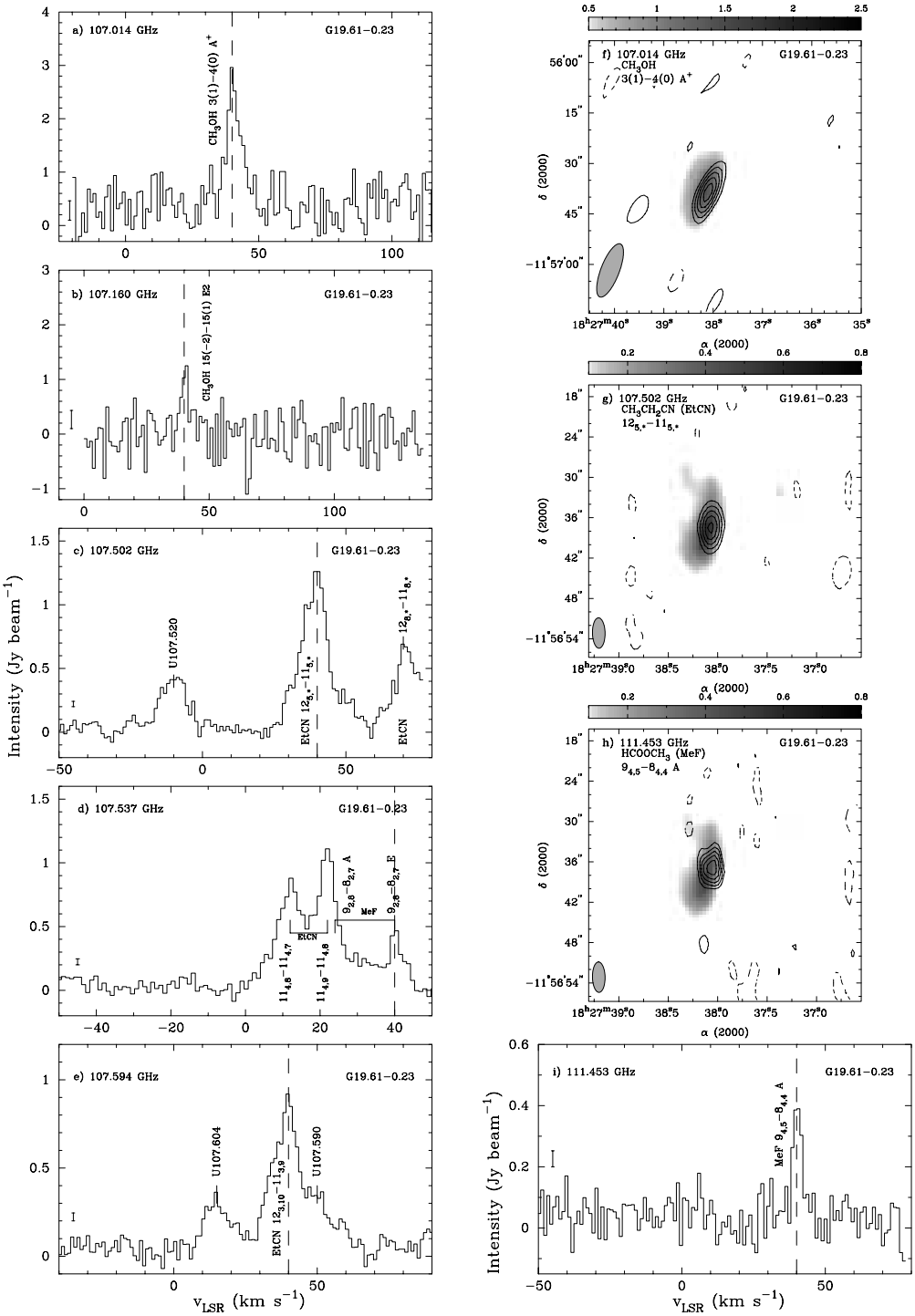

FIG. 3.—(*a*–*e*) Spectrum taken toward G19.61−0.23 showing several detections of CH_3OH, CH_3CH_2CN (EtCN), and $HCOOCH_3$ (MeF). The rms noise level is indicated by the vertical bar at the left of the spectrum. The spectral line labels correspond to the rest frequency located at the top left of each panel for a v_{LSR} of 40 km s^{-1} (*dashed line*). (*f*) Emission contours from the 3(1)–4(0) A^+ transition of CH_3OH at 107.014 GHz at the emission peak of 40 km s^{-1} overlaid on the G19.61−0.23 continuum emission at 107.0 GHz (*gray scale*). The numbers on the gray scale wedge are in units of Jy beam^{-1}. The CH_3OH contour levels are −0.10, 0.10, 0.15, 0.20, 0.25, 0.30, and 0.35 Jy beam^{-1}. The synthesized beam of $16\farcs9 \times 5\farcs5$ is indicated at the bottom left corner. (*g*) Emission contours from the $12_{5,*}-11_{5,*}$ transition of CH_3CH_2CN at 107.502 GHz at the emission peak of 40 km s^{-1} overlaid on the G19.61−0.23 continuum emission at 107.5 GHz (*gray scale*). The CH_3CH_2CN contour levels are −0.1, 0.4, 0.6, 0.8, 1.0, and 1.2 Jy beam^{-1}. The synthesized beam of $4\farcs7 \times 1\farcs9$ is indicated at the bottom left corner. (*h*) Emission contours from the $9_{4,5}-8_{4,4}$ A transition of $HCOOCH_3$ at 111.453 GHz at the emission peak of 40 km s^{-1} overlaid on the G19.61−0.23 continuum emission at 111.5 GHz (*gray scale*). The $HCOOCH_3$ contour levels are −0.10, 0.15, 0.20, 0.25, 0.30, and 0.35 Jy beam^{-1}. The synthesized beam of $4\farcs7 \times 1\farcs9$ is indicated at the bottom left corner. (*i*) Spectrum showing the 111.453 GHz transition of $HCOOCH_3$. The labels are the same as in (*a*).

from the hot core region was optically thick and that corrections needed to be made in order to more accurately determine $T_{\rm rot}$ and $N_{\rm tot}$. Remijan et al. (2004) made an extensive study of CH_3CN toward the hot core regions W51 e1 and e2. In that analysis, they corrected for optical depth, and the results from the RTD analysis closely matched the statistical equilibrium analysis. Furthermore, they found CH_3CN is a good tracer of large hard-to-detect species such as CH_3COOH. In this analysis, we reexamined the CH_3CN data from Watson et al. (2002) and investigated how well CH_3CN traces larger molecular species.

3. RESULTS

The three sources in Table 3 were surveyed for CH_3COOH, as well as the selected transitions of other large molecular species listed in Table 2. Figure 1 summarizes the CH_3COOH (acetic acid [AcA]) survey toward each region. The spectral line labels located at the upper left of each panel correspond to the rest frequency for the $v_{\rm LSR}$ of each source (40 km s^{-1} for G19.61−0.23, 62 km s^{-1} for G45.47+0.05, and 10 km s^{-1} for W75N). The 1 σ noise level is shown at the left of each spectrum. No new sources of CH_3COOH were detected. We did make the first detections of HCOOH, $HCOOCH_3$, and CH_3CH_2CN toward G19.61−0.23 and HCOOH and $HCOOCH_3$ toward W75N. Finally, we detected CH_3CN emission from all the sources and were able to measure the column density of the detected molecular species and, based on the 1 σ detection limit, place upper limits on the species that were not detected. In § 3.1, we discuss the spectral lines detected toward G19.61−0.23. In §§ 3.2 and 3.3, we discuss the spectral lines detected toward G45.47+0.05 and W75N, respectively.

3.1. *G19.61−0.23*

Figure 2*a* shows the first detection of HCOOH toward G19.61−0.23. The spectral line label located in the upper left of Figure 2*a* corresponds to the rest frequency for a $v_{\rm LSR}$ of 40 km s^{-1}. The 1 σ noise level is shown at the left of the spectral window. Figure 2*b* shows the map of the $5_{1,5}$–$4_{1,4}$ transition of formic acid (*contours*) on top of the 108.1 GHz continuum emission (*gray scale*). Note that the emission peak of HCOOH is offset from the continuum emission. The offset in emission peaks is significant, given the size of the synthesized beam (shown at the bottom left of Fig. 2*b*). Figure 3 shows the detection and distribution of several large molecular species toward the G19.61−0.23 region, including CH_3OH, CH_3CH_2CN (EtCN), and $HCOOCH_3$ (MeF). Figures 3*a* and 3*b* show the detection of CH_3OH at 107.014 and 107.160 GHz, respectively. The spectral line labels are similar to those of Figure 2*a*. Figure 3*f* shows the distribution of the 107.014 GHz CH_3OH emission (*contours*) on the 3 mm continuum emission (*gray scale*) toward G19.61−0.23. Figures 3*c*–3*e* show the detections of several transitions of CH_3CH_2CN. Figure 3*g* shows the distribution of the 107.502 GHz CH_3CH_2CN emission. Finally, Figures 3*d* and 3*i* show the detections of three transitions of $HCOOCH_3$. Figure 3*h* shows the distribution of the 111.453 GHz $HCOOCH_3$ emission. Figure 4 shows the detection and distribution of CH_3CN toward the G19.61−0.23 region. In Figure 4*f* we show the predicted locations of the $J = 6$–5, $K = 0$, 1, 2 and 3 $CH_3^{13}CN$ emission lines. While the $K = 3$ line is clearly seen near $v_{\rm LSR}$ of 148 km s^{-1}, the lower K-value transitions are not as clearly seen. However, we note that as much as 50% of the emission from the $K = 5$ CH_3CN line may be due to the $K = 0$ and 1 $CH_3^{13}CN$ lines. Higher signal-to-noise ratio observations are needed to confirm the amount of contamination from $CH_3^{13}CN$. The peak positions of CH_3CN, CH_3OH, HCOOH, CH_3CH_2CN, and $HCOOCH_3$ agree, strongly indicating that all the molecular emission is coming from a common source. Table 4 lists the molecular species that were detected toward G19.61−0.23 at or near the systemic velocity (40 km s^{-1}). Least-squares Gaussian fits were made for each spectral line in order to obtain the radial velocities and integrated line intensities for the detected transitions. In Table 4, column (1) lists either the calculated rest frequencies of previously identified species or the observed frequencies of unidentified transitions. Columns (2) and (3) list the molecular species and associated transitions, respectively. Finally, column (4) lists the fitted integrated line intensity of each detected transition.

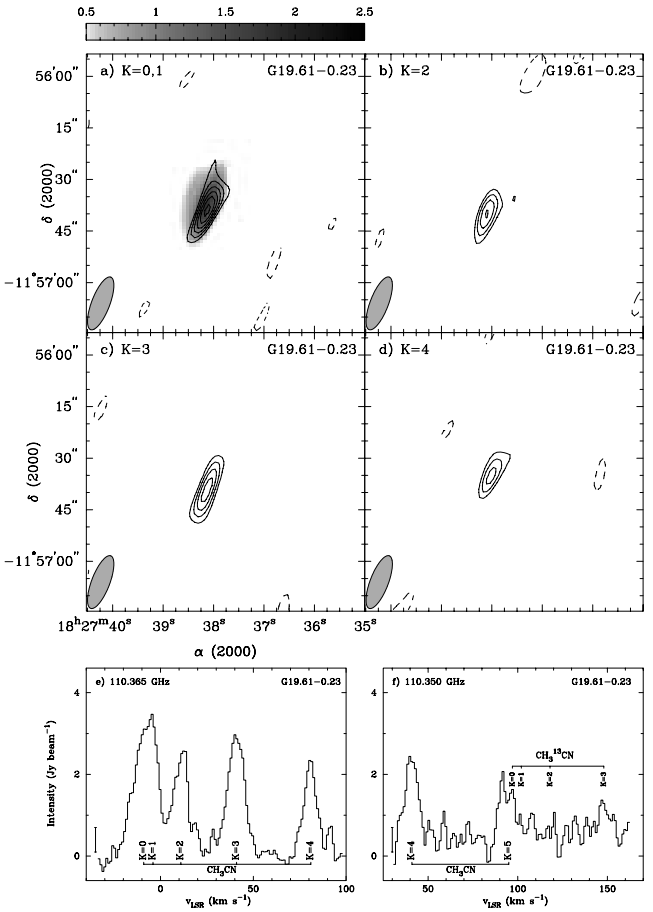

FIG. 4.—(*a*–*d*) Averaged intensity maps of the $J = 6$–5 CH_3CN emission lines. The gray scale in (*a*) is for the 110.4 GHz continuum of the G19.61−0.23 region. The numbers on the gray scale wedge are in units of Jy beam^{-1}. In each panel, the given K-ladder transition taken at the peak velocity of the line is mapped in contours. The contour levels are −1.0, 1.5, 2.0, 2.5, 3.0, 3.5, and 4.0 Jy beam^{-1}. The synthesized beam of 16.″4 × 5.″3 is indicated at the bottom left of each panel. (*e*) CH_3CN spectrum taken toward the G19.61−0.23 region. The rest frequency located in the top left corner corresponds to the $K = 3$ component for a $v_{\rm LSR}$ of 40 km s^{-1}. The noise level is ∼0.6 Jy beam^{-1} (indicated by the vertical bar at the left of the spectrum). (*f*) Same as (*e*) except the rest frequency corresponds to the $K = 4$ component. Also shown are the predicted locations of the $J = 6$–5, $K = 0$, 1, 2, and 3 $CH_3^{13}CN$ emission lines. The $K = 3$ line is clearly seen near $v_{\rm LSR}$ of 148 km s^{-1}.

3.2. *G45.47+0.05*

Figure 5 shows the results of our survey toward G45.47+0.05. Of the seven molecular species searched for, we only

TABLE 4
G19.61−0.23 Molecular Line Identifications

Frequency[a] (MHz) (1)	Species (2)	Transition (3)	$\int \Delta I\, dv$[b] (Jy beam^{-1} km s^{-1}) (4)
107,013.850 ± 100	CH_3OH	3(1)–4(0) A^+	24.1 ± 3.9
107,159.790 ± 100	CH_3OH	15(−2)–15(1) E2	4.5 ± 1.7
107,491.573 ± 28	EtCN[c]	$12_{8,*}-11_{8,*}$	7.8 ± 6
107,502.426 ± 26	EtCN	$12_{5,*}-11_{5,*}$	14.7 ± 8
107,520.0	U107.520		5.3 ± 5
107,537.189 ± 24	MeF[d]	$9_{2,8}-8_{2,7}$ E	3.1 ± 3
107,543.746 ± 26	MeF	$9_{2,8}-8_{2,7}$ A	3.1 ± 1.0[e]
107,543.926 ± 26	EtCN	$12_{4,9}-11_{4,8}$	5.5 ± 1.0[e]
107,547.601 ± 26	EtCN	$12_{4,8}-11_{4,7}$	6.6 ± 4
107,590.0	U107.590		3.2 ± 5[e]
107,594.049 ± 28	EtCN	$12_{3,10}-11_{3,9}$	10.0 ± 6[e]
107,604.0	U107.604		3.9 ± 4
108,126.710 ± 160	HCOOH	$5_{1,5}-4_{1,4}$	1.5 ± 3
110,309.847 ± 10	$CH_3^{13}CN$	6(3)–5(3)	13.1 ± 3.0
110,329.608 ± 120	CH_3CN	6(5)–5(5)	16.3 ± 2.1[e]
110,349.760 ± 200	CH_3CN	6(4)–5(4)	22.5 ± 2.0
110,364.470 ± 100	CH_3CN	6(3)–5(3)	33.8 ± 2.3
110,374.986 ± 120	CH_3CN	6(2)–5(2)	26.4 ± 2.1
110,381.376 ± 120	CH_3CN	6(1)–5(1)	23.8 ± 3.0[e]
110,383.494 ± 120	CH_3CN	6(0)–5(0)	25.8 ± 3.0[e]
111,453.327 ± 24	MeF	$9_{4,5}-8_{4,4}$ A	1.8 ± 3
111,526.0	U111.526		0.5 ± 2

[a] Errors are 2 σ.
[b] Errors are 1 σ.
[c] EtCN = ethyl cyanide (CH_3CH_2CN).
[d] MeF = methyl formate ($HCOOCH_3$).
[e] Blended line.

detected emission from one transition of CH_3OH and four transitions of CH_3CN. Figure 5*a* shows the detection of the 3(1)–4(0) A^+ transition of CH_3OH toward G45.47+0.05. The spectral line label located in the upper left of Figure 5*a* corresponds to the rest frequency for a v_{LSR} of 62 km s^{-1}. The 1 σ noise level is shown at the left of the spectral window. Figure 5*b* shows the map of the 3(1)–4(0) A^+ transition of CH_3OH (*contours*) on top of the 107.0 GHz continuum emission (*gray scale*). In this case, significant differences between the continuum peak and the CH_3OH emission peak are not seen. Figures 5*c*–5*f* show the average intensity maps and spectrum of the four detected transitions of the $J = 6$–5 CH_3CN emission lines. Once again, no offsets are seen between the CH_3CN emission peak and the 110.5 GHz continuum peak. However, from Figure 5*c* there appears to be at least two additional emission peaks of CH_3CN, one to the southeast and one to the northwest. The peaks also appear in the $K = 1$ window; however, we also see emission coming from the southwest. In the $K = 3$ window, only the CH_3CN emission peak near the continuum is present. From the fitting routine to measure source sizes (§ 4.1), we found that this region may contain several molecular cores. Higher signal-to-noise ratio observations are necessary to identify the number of individual cores toward this region. Table 5 lists the molecular species that were detected toward G45.47+0.05 at or near the systemic velocity (62 km s^{-1}). The column labels are the same as in Table 4.

3.3. *W75N*

Figure 6 shows the first detections of $HCOOCH_3$ and HCOOH toward W75N. Figure 6*a* shows the detection of the $9_{2,8}-8_{2,7}$ A and E transitions of $HCOOCH_3$ near 107.5 GHz. The spectral line labels correspond to the rest frequency located at the upper left of the panel for a v_{LSR} of 10 km s^{-1}. The 1 σ noise level is shown at the left of the spectrum. Figure 6*b* shows the map of the $9_{2,8}-8_{2,7}$ E transition of $HCOOCH_3$ (*contours*) on top of the 107.5 GHz continuum emission (*gray scale*). Note that the emission peak of $HCOOCH_3$ is offset from the continuum emission. The offset in emission peaks is significant, given the size of the synthesized beam (seen at the bottom left of Fig. 6*b*). Figure 6*c* shows the detection of the $5_{1,5}-4_{1,4}$ transition of HCOOH at 108.1 GHz. This is the first time any large oxygen-bearing molecule has been detected toward W75N. Furthermore, we do not detect any large nitrogen-bearing molecules, such as CH_3CH_2CN, in this region. Figure 7 shows the average intensity maps and spectrum of the $J = 6$–5 CH_3CN emission lines. From these maps, we see the CH_3CN emission is extended beyond the $2\farcs7 \times 2\farcs2$ synthesized beam (*shown at the bottom left of each panel*) but peaks near the continuum. The peaks of the emission contours of CH_3CN and $HCOOCH_3$ are offset by $\sim 2\farcs7$, indicating that the molecular emission is coming from at least two distinct sources. Table 6 lists the molecular species that were detected toward W75N at or near the systemic velocity (10 km s^{-1}). The column labels are the same as in Table 4.

4. DISCUSSION

4.1. *Rotational Temperature Diagrams of* CH_3CN

One of the most difficult factors to determine is the column densities of large biomolecules in the interstellar medium. By measuring the column densities of biomolecules in many different regions with various physical conditions, we can get a

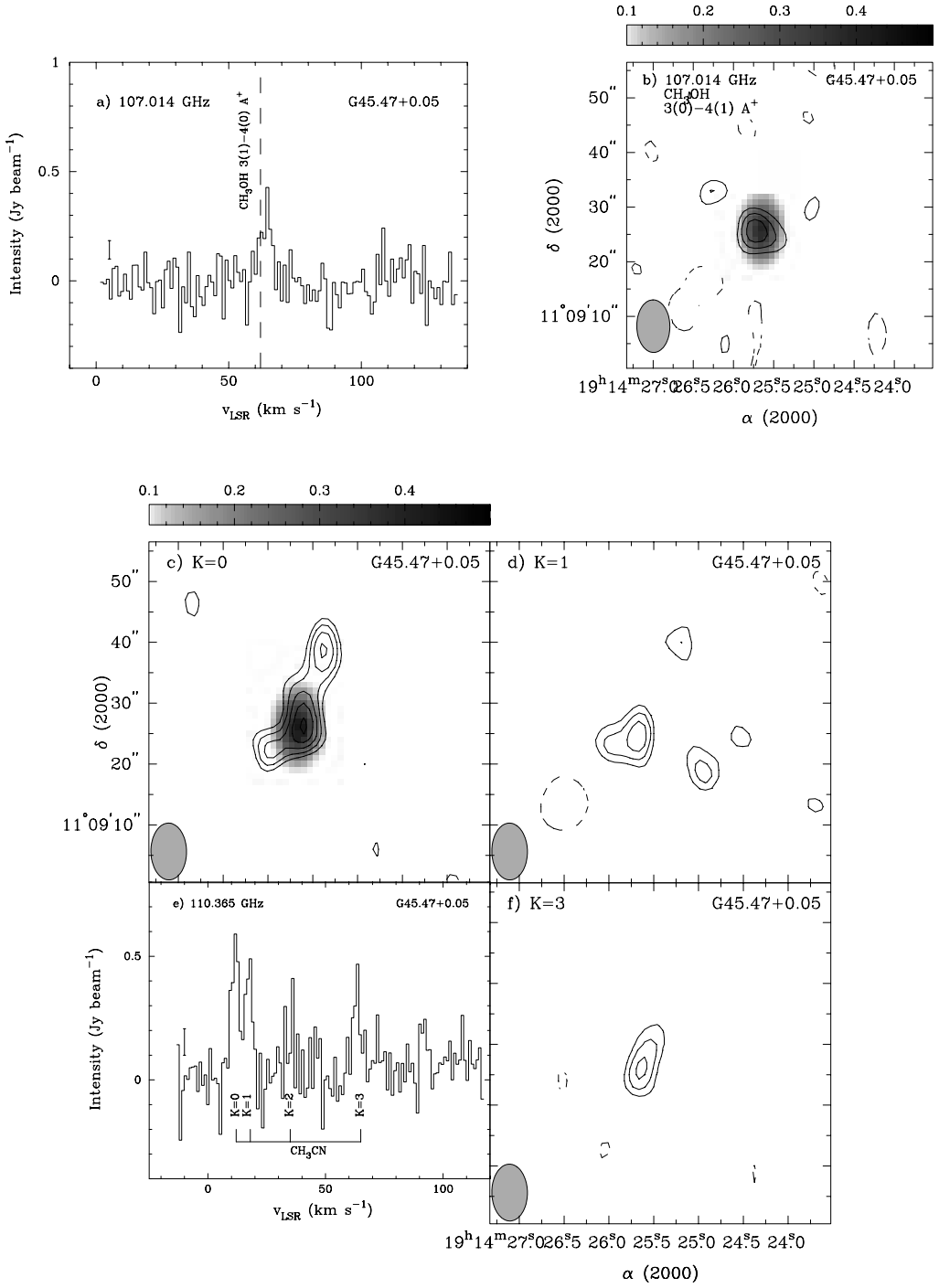

FIG. 5.—(*a*) CH_3OH spectrum toward G45.47+0.05. The noise level is ~84 mJy beam^{-1} (indicated by the vertical bar at the left of the spectrum). The spectral line label corresponds to the rest frequency located at the top left of the panel for a v_{LSR} of 62 km s^{-1} (*dashed line*). (*b*) Emission contours from the 3(1)–4(0) A^+ transition of CH_3OH at 107.014 GHz overlaid on the G45.47+0.05 continuum emission at 107.0 GHz (*gray scale*). The numbers on the gray scale wedge are in units of Jy beam^{-1}. Contours indicate the location of the CH_3OH emission near its peak at 65 km s^{-1}. The contour levels are −0.15, 0.225, 0.30, 0.375, 0.45, and 0.525 Jy beam^{-1}. The synthesized beam of 9.″6 × 6.″1 is indicated at the bottom left corner. (*c–f*) Averaged intensity maps and spectrum of the $J = 6-5$ CH_3CN emission lines. The gray scale in (*c*) is for the 110.4 GHz continuum of the G45.47+0.05 region. The numbers on the gray scale wedge are in units of Jy beam^{-1}. In each panel, the given *K*-ladder transition taken at the peak velocity of the line is mapped in contours. The contour levels are −0.3, 0.3, 0.375, 0.45, 0.525, 0.60, and 0.75 Jy beam^{-1}. The synthesized beam of 9.″3 × 5.″8 is indicated at the bottom left of each panel.

better understanding of their formation mechanism, distribution, and relative abundance compared with other large molecular species.

There are three primary procedures used in calculating the total beam-averaged column density of a particular molecular species. They are the rotational temperature diagram method (RTDM; Goldsmith & Langer 1999), the statistical equilibrium method (SEM), and the assumption of LTE. The methods are outlined in detail in Remijan et al. (2004). With the exception of CH_3CN, not enough transitions with a wide spread of upper-state energy levels have been observed to utilize the RTDM. Furthermore, because many of our species are asymmetric top molecules, detailed collision rates are not known, so we cannot utilize the SEM. In the case of CH_3CN, we can use the RTDM

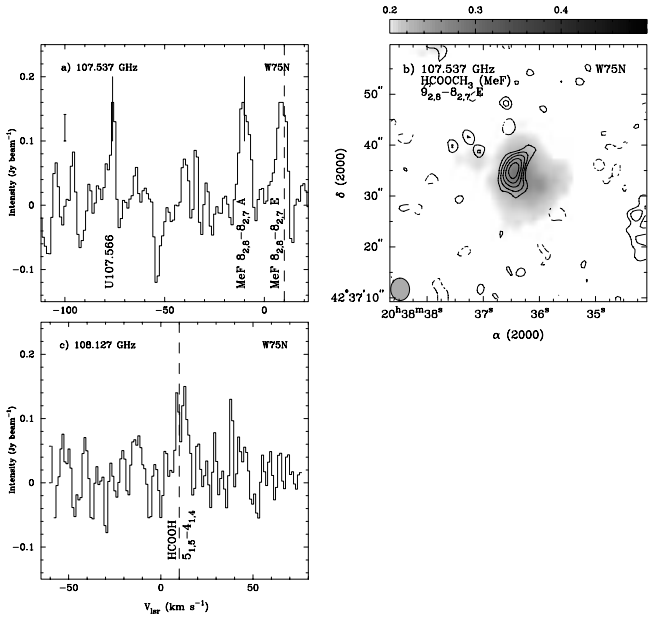

FIG. 6.—(*a*) $HCOOCH_3$ spectrum toward W75N. The noise level is ~40 mJy beam^{-1} (indicated by the vertical bar at the left of the spectrum). The spectral line label corresponds to the rest frequency located at the top left of the panel for a v_{LSR} of 10 km s^{-1} (*dashed line*). (*b*) Emission contours from the $9_{2,8}-8_{2,7}$ E transition of $HCOOCH_3$ at 107.537 GHz overlaid on the W75N continuum emission at 107.5 GHz (*gray scale*). The numbers on the gray scale wedge are in units of Jy beam^{-1}. Contours indicate the location of the $HCOOCH_3$ emission near its peak at 10 km s^{-1}. The contour levels are −0.1, 0.1, 0.15, 0.20, 0.25, and 0.30 Jy beam^{-1}. The synthesized beam of $4''.4 \times 3''.7$ is indicated at the bottom left corner. (*c*) HCOOH spectrum toward W75N. The spectral line labels are the same as in (*a*).

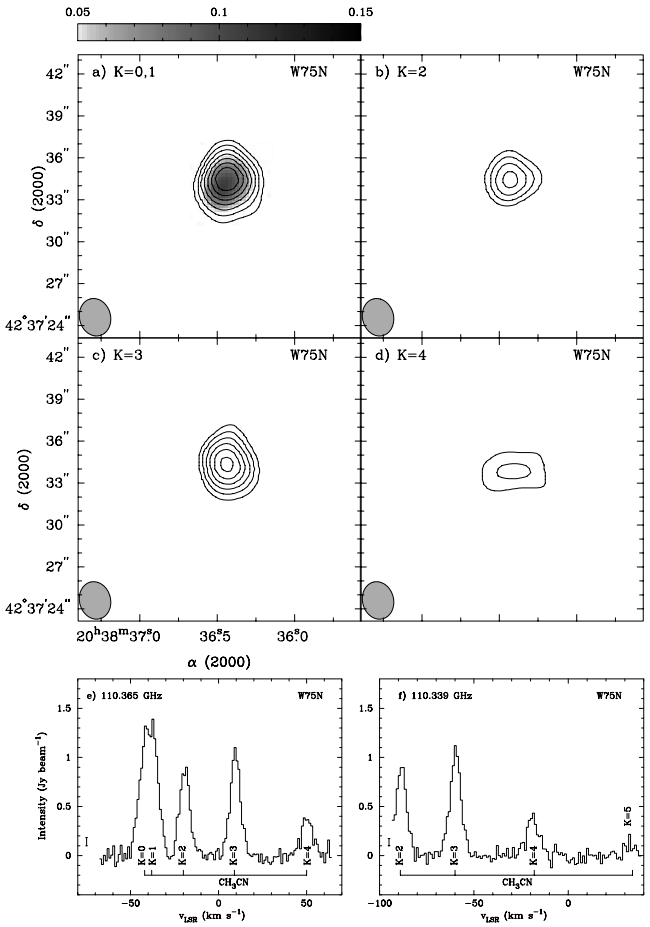

FIG. 7.—Same as Fig. 4, but toward W75N. The contour levels are 0.4, 0.5, 0.6, 0.7, 0.8, and 1.0 Jy beam^{-1} except in (*d*), where the contour levels are 0.2 and 0.3 Jy beam^{-1}. The synthesized beam of $2''.7 \times 2''.2$ is indicated at the bottom left corner of each panel.

to determine a rotational temperature and the column density. If the CH_3CN population can be described by a single rotational temperature and if all the lines are optically thin, the measured intensities are proportional to the column densities in the upper levels of the transitions being observed. From Remijan et al. (2004), we have

$$\frac{N_u}{g_u} = 2.04 \frac{\int \Delta I \, dv}{\Omega_s \nu^3 S_{ij}\mu^2} \times 10^{20} \text{ cm}^{-2}, \quad (1)$$

$$\frac{N_u}{g_u} = \frac{N_{\rm tot}}{Q(T_{\rm rot})} e^{-(E_u/kT_{\rm rot})}, \quad (2)$$

where N_u is the upper level column density, g_u is the statistical weight of the upper level, Ω_s is the solid angle subtended by the source (arcsec^2), $\int \Delta I \, dv$ is the integrated line intensity (Jy beam^{-1} km s^{-1}), ν is the rest frequency (GHz), $S_{ij}\mu^2$ is the product of the total torsional-rotational line strength and the square of the electric dipole moment (D^2), and, in equation (2), $N_{\rm tot}$ is the total source-averaged column density, $Q(T_{\rm rot})$ is the rotational partition function, E_u is the upper-state energy level, and $T_{\rm rot}$ is the rotational temperature. One can thereby determine the rotational temperature from the slope of the fit and

TABLE 5

G45.47+0.05 MOLECULAR LINE IDENTIFICATIONS

Frequency[a] (MHz)	Species	Transition	$\int \Delta I \, dv$[b] (Jy beam^{-1} km s^{-1})
107,013.850 ± 100.....	CH_3OH	3(1)–4(0) A$^+$	1.7 ± 7
110,364.470 ± 100.....	CH_3CN	6(3)–5(3)	1.6 ± 3
110,374.986 ± 120.....	CH_3CN	6(2)–5(2)	0.9 ± 3
110,381.376 ± 120.....	CH_3CN	6(1)–5(1)	1.9 ± 3
110,383.494 ± 120.....	CH_3CN	6(0)–5(0)	2.3 ± 4

[a] Errors are 2 σ.
[b] Errors are 1 σ.

TABLE 6

W75N MOLECULAR LINE IDENTIFICATIONS

Frequency[a] (MHz)	Species	Transition	$\int \Delta I \, dv$[b] (Jy beam^{-1} km s^{-1})
107,537.189 ± 24.....	MeF[c]	$9_{2,8}-8_{2,7}$ E	0.8 ± 1[d]
107,543.746 ± 26.....	MeF	$9_{2,8}-8_{2,7}$ A	0.7 ± 1[d]
107,566.0.....	U107.566	...	0.5 ± 1[d]
108,126.710 ± 160.....	HCOOH	$5_{1,5}-4_{1,4}$	0.6 ± 1[d]
110,329.608 ± 120.....	CH_3CN	6(5)–5(5)	0.8 ± 2[e]
110,349.760 ± 200.....	CH_3CN	6(4)–5(4)	2.9 ± 2
110,364.470 ± 100.....	CH_3CN	6(3)–5(3)	7.6 ± 3
110,374.986 ± 120.....	CH_3CN	6(2)–5(2)	6.4 ± 2
110,381.376 ± 120.....	CH_3CN	6(1)–5(1)	7.6 ± 4[e]
110,383.494 ± 120.....	CH_3CN	6(0)–5(0)	7.6 ± 4[e]

[a] Errors are 2 σ.
[b] Errors are 1 σ.
[c] MeF: methyl formate ($HCOOCH_3$).
[d] The intensity and line width were approximated because the least-squares Gaussian fitting routine did not give a satisfactory fit.
[e] Blended line.

TABLE 7
SOURCE SIZE MEASUREMENTS

Source (1)	Species (2)	Transition (3)	Size (arcsec^2) (4)
G19.61−0.23.....	CH_3CN	6(0)–5(0)	60.9 ± 6.0[a]
	CH_3CN	6(1)–5(1)	60.9 ± 6.0[a]
	CH_3CN	6(2)–5(2)	31.8 ± 3.2
	CH_3CN	6(3)–5(3)	15.5 ± 3.0
	CH_3CN	6(4)–5(4)	64.8 ± 15.1
	EtCN	$12_{8,*}-11_{8,*}$	2.9 ± 2
	EtCN	$12_{5,*}-11_{5,*}$	1.7 ± 3
	EtCN	$12_{4,8}-11_{4,7}$	3.6 ± 2
	EtCN	$12_{3,10}-11_{3,9}$	2.6 ± 1
	EtCN	$12_{4,9}-11_{4,8}$	2.2 ± 1[a]
	MeF	$9_{2,8}-8_{2,7}$ A	2.2 ± 1[a]
	MeF	$9_{2,8}-8_{2,7}$ E	2.4 ± 5
	MeF	$9_{4,5}-8_{4,4}$ A	3.8 ± 6
	HCOOH	$5_{1,5}-4_{1,4}$	Point source
	CH_3OH	3(1)–4(0) A^+	Point source
G45.47+0.05	CH_3CN	6(0)–5(0)	243.1 ± 35.5
	CH_3CN	6(1)–5(1)	294.2 ± 151.2
	CH_3CN	6(3)–5(3)	189.4 ± 43.4
	CH_3OH	3(1)–4(0) A^+	65.4 ± 6.0
W75N.....	CH_3CN	6(0)–5(0)	11.3 ± 3[a]
	CH_3CN	6(1)–5(1)	11.3 ± 3[a]
	CH_3CN	6(2)–5(2)	8.8 ± 3
	CH_3CN	6(3)–5(3)	8.8 ± 3
	CH_3CN	6(4)–5(4)	10.1 ± 1.1
	CH_3CN	6(4)–5(4)	12.7 ± 5.0
	MeF	9(2,8)–8(2,7) A	19.8 ± 2
	MeF	9(2,8)–8(2,7) E	7.2 ± 2

[a] Blended line.

an estimate of the total molecular column density from the y-intercept. In order to measure Ω_s and construct accurate RTDs, we need a CH_3CN source size for each region. Source sizes are determined for the detected transitions assuming a Gaussian distribution and are summarized in Table 7. In column (1) we list the source. Columns (2) and (3) list the molecular species and associated transition, respectively. Column (4) lists the source size deconvolved from the synthesized beam determined from that transition along with its 1 σ error. From this analysis, we find an average source size of 43.3 ± 8.4 arcsec^2 for CH_3CN, 2.6 ± 2 arcsec^2 for CH_3CH_2CN, and 2.8 ± 4 arcsec^2 for $HCOOCH_3$ toward G19.61−0.23. Toward G45.47+0.05, we find an average source size of 242.2 ± 80.6 arcsec^2 for CH_3CN and 65.4 ± 6.0 arcsec^2 for CH_3OH. Toward W75N, we find an average source size of 10.3 ± 2.6 arcsec^2 for CH_3CN and 13.5 ± 2.0 arcsec^2 for $HCOOCH_3$. Using these values, we constructed RTDs using CH_3CN for each source. The results are shown in Figure 8. In each diagram, optical depth corrections were made using the procedure outlined in Remijan et al. (2004).

Figure 8*a* shows the RTD of CH_3CN toward G45.47+0.05. We were only able to detect four K-components in the $J = 6$–5 ladder. From the RTD, we find a rotational temperature of 81 ± 63 K and a total source-averaged column density of $N_{\rm tot} = (1.9 \pm 2.3) \times 10^{13}$ cm^{-2}. It is apparent from the spectrum shown in Figure 5 that the CH_3CN emission is optically thin ($\tau < 0.003$). Given the lower rotational temperature and the highly extended (>240 arcsec^2) nature of the emission, it appears that CH_3CN may contain several individual cores that trace a cooler component of molecular gas. Figure 8*b* shows

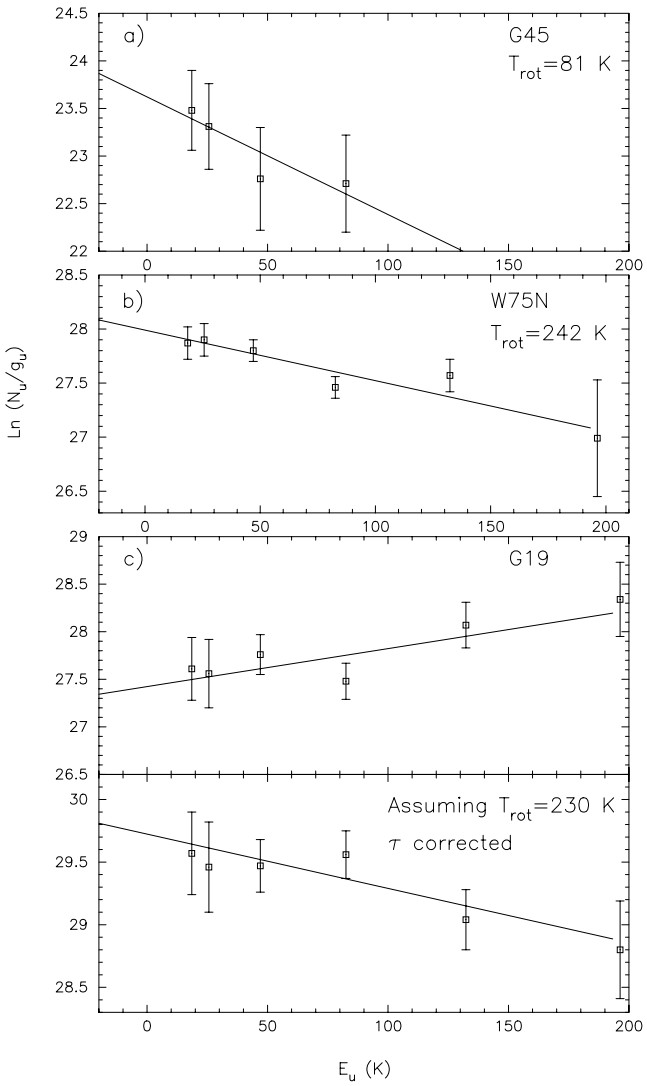

FIG. 8.—(*a*) Rotational temperature diagram for the observed CH_3CN transitions toward G45.47+0.05. *Ordinate*: $\ln(N_u/g_u)$. *Abscissa*: $E_u(K)$. The least-squares fit across K-levels is shown as a solid line. The resulting rotational temperature is 81 K. (*b*) Rotational temperature diagram for the observed CH_3CN transitions toward W75N. The resulting rotational temperature is 242 K. (*c*) Rotational temperature diagram for the observed CH_3CN transitions toward G19.61−0.23. In this case, the diagram gives a nonphysical rotational temperature. Below, the rotational temperature diagram assuming a temperature of 230 K and correcting for optical depth effects.

the RTD for all six K-components in the $J = 6$–5 ladder toward W75N. From the diagram, we find a rotational temperature of 242 ± 84 K and a total source-averaged column density of $N_{\rm tot} = (7.5 \pm 3.9) \times 10^{15}$ cm^{-2}. Furthermore, the emission is very compact (∼10 arcsec^2); however, the optical depth of these lines is no greater than 0.06. Toward W75N, we are clearly detecting a HMC region unlike that seen toward G45.47+0.05. Finally, Figure 8*c* shows the RTD toward G19.61−0.23. In this case, we see the CH_3CN emission is optically thick, and we obtain a nonphysical rotational temperature. Therefore, the standard procedure of iteratively making corrections to the RTD cannot be applied in this case. However, if we assume $T_{\rm rot} = 230$ K (Kurtz et al. 2000), we can make optical depth corrections by changing the column density until the slope of the RTD gives a temperature of 230 K. Using this method, we find a total source-averaged column density of $N_{\rm tot} = 1.6 \times 10^{18}$ cm^{-2} and optical depth values as large as

8.0 in the $K = 3$ transition. This opacity-corrected rotation diagram assuming a temperature of 230 K is also shown in Figure 8*c*. However, the total column density value should only be considered an approximation, and in order to truly measure the temperature, the column density of CH_3CN, and H_2 density toward this region, a full statistical equilibrium analysis needs to be applied.

4.2. *Column Densities of Large Molecular Species in G19.61−0.23*

In order to determine the column densities of the remaining large molecules, we adopted the temperature reported by Kurtz et al. (2000) of 230 K and assumed LTE excitation. Figure 9 and Table 8 summarize the total source-averaged column densities, fractional abundances, and upper limits of all the large molecular species toward each high-mass SFR. In Table 8, the source for each column density measurement is given in column (1). Columns (2), (3), (4), and (5) list the total source-averaged column densities for HCOOH, $HCOOCH_3$, CH_3CH_2CN, and CH_3COOH, respectively. Assuming a temperature of 230 K, we find an average total source-averaged column density of $N_{\rm tot} = 9.3 \times 10^{16}$ cm^{-2} for CH_3CH_2CN and $N_{\rm tot} = 3.4 \times 10^{17}$ cm^{-2} for $HCOOCH_3$. For HCOOH, we find a total source-averaged column density of $N_{\rm tot} = 6.0 \times 10^{16}$ cm^{-2}. Using this same procedure for our CH_3CN lines, we find a total source-averaged column density of $N_{\rm tot} = 6.8 \times 10^{15}$ cm^{-2}. Finally, using the 1 σ noise level of our combined data set, we were able to set an upper limit to the total column density of $N_{\rm tot} = 3.0 \times 10^{16}$ cm^{-2} for CH_3COOH. This gives a relative $CH_3COOH/HCOOCH_3$ abundance ratio of less than 9×10^{-2} for G19.61−0.23. This is higher than the abundance ratio found toward Sgr B2(N-LMH), W51e2, and G34.3+0.2 [$(3–7) \times 10^{-2}$], but this is still an upper limit (Remijan et al. 2003). The relative $HCOOH/HCOOCH_3$ abundance ratio is 0.18, which is comparable to the abundance ratios found by Liu et al. (2001) toward Sgr B2(N-LMH), Orion, and W51 ($\sim$0.10). For the two transitions of CH_3OH, we can use the same procedure to calculate an average CH_3OH total source-averaged column density of $N_{\rm tot} = 2.0 \times 10^{18}$ cm^{-2}. However, both are maser transitions of CH_3OH, so the column density determined from equation (1) is not valid in this case and should be considered only as an upper limit. From our observations, it appears that the hot core regions toward the G19.61−0.23 region are very similar to the hot cores in G34.3+0.2. In fact, the measured column densities of $HCOOCH_3$ and CH_3CH_2CN are higher toward G19.61−0.23 than G34.3+0.2 (Remijan et al. 2003). We conclude that the nondetection of CH_3COOH toward this region is signal-to-noise limited and that a deeper survey should detect emission of CH_3COOH. In fact, in Figure 1*a*, there is a suggestion that the 111.507 GHz line of CH_3COOH is starting to be resolved out of the noise.

4.3. *Column Densities of Large Molecular Species in W75N and G45.47+0.05*

In total, we observed two transitions of $HCOOCH_3$ toward W75N, one transition of HCOOH toward W75N, and one transition of CH_3OH toward G45.47+0.05. For the transition of CH_3OH toward G45.47+0.05 using the rotational temperature of 81 K from the RTDM of CH_3CN, we find a CH_3OH total source-averaged column density of $N_{\rm tot} = 1.8 \times 10^{15}$ cm^{-2}. However, this is a maser transition of CH_3OH, so the column density determined should once again only be considered an upper limit. For $HCOOCH_3$ toward W75N using the rotational temperature of 242 K from the RTDM of CH_3CN, we find an average total source-averaged column density of $N_{\rm tot} = 2.1 \times 10^{16}$ cm^{-2}, and for HCOOH, we find a total source-averaged column density of $N_{\rm tot} = 5.4 \times 10^{15}$ cm^{-2}. The relative $HCOOH/HCOOCH_3$ abundance ratio is 0.26, which is more than twice as large as the abundance ratios found by Liu et al. (2001). Figure 9 graphically summarizes the column densities and upper limit column densities of CH_3COOH, CH_3CH_2CN, HCOOH, CH_3CN, and $HCOOCH_3$ toward G19.61−0.23, G45.47+0.05, and W75N. Toward G45.47+0.05, we did not detect emission from any other large molecular species except for CH_3OH and CH_3CN. The emission from both species is highly extended, greater than 60 arcsec^2 for CH_3OH and greater than 240 arcsec^2 for CH_3CN, and the temperature determined from the RTDM is only 81 K with a large error (63 K). Thus, it appears that G45.47+0.05 does not contain a compact HMC that contains the physical conditions suitable to form large molecular species. In fact, the G45.47+0.05 region may contain a chemistry similar to that of cold dark clouds. Further observations that compare the chemistry of these regions are necessary to confirm this hypothesis.

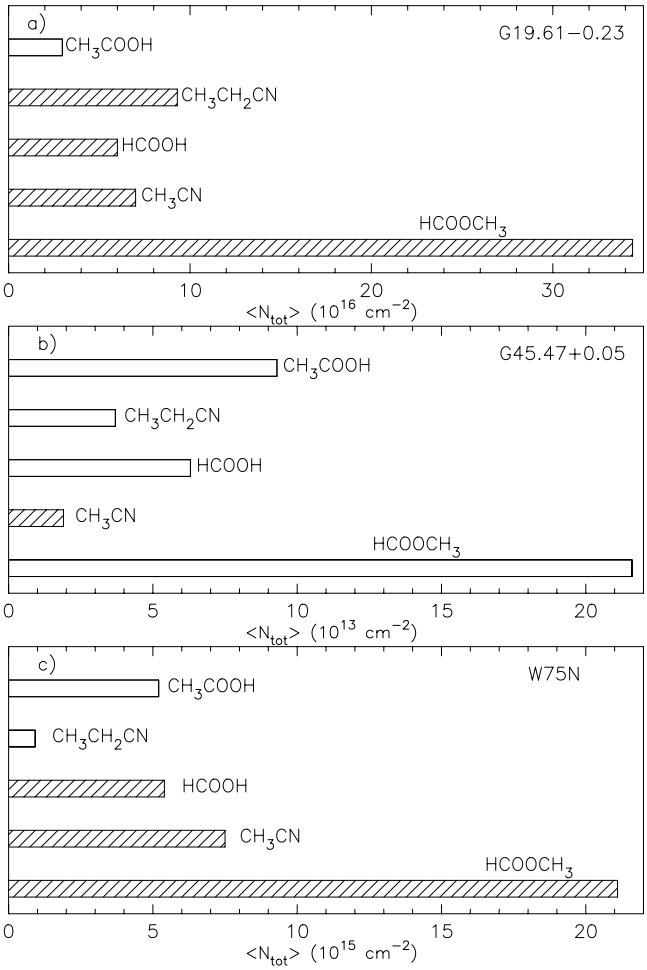

FIG. 9.—(*a*) Beam-averaged column densities determined from G19.61−0.23 interferometric measurements. The unhatched bars indicate upper limits to the column density measurements; the hatched bars indicate measured column densities based on optically thin emission assuming LTE excitation. (*b*) Beam-averaged column densities determined from G45.47+0.05 interferometric measurements. (*c*) Beam-averaged column densities determined from W75N interferometric measurements.

W75N does contain hot cores, but these observations suggest for the first time that there is a differentiation between the O and N cores toward this region. The emission from

TABLE 8
Column Densities and Fractional Abundances

Source (1)	N_{HCOOH} (10^{15} cm^{-2}) (2)	N_{HCOOCH_3} (10^{15} cm^{-2}) (3)	$N_{CH_3CH_2CN}$ (10^{15} cm^{-2}) (4)	N_{CH_3COOH} (10^{15} cm^{-2}) (5)
G19.61−0.23.....	60.2	344.5	93.3	<29.6
G45.47+0.05.....	<0.06	<0.22	<0.04	<0.09
W75N.....	5.4	21.1	<0.92	<5.17

Source	X_{HCOOH} ($\times10^{-8}$)	X_{HCOOCH_3} ($\times10^{-8}$)	$X_{CH_3CH_2CN}$ ($\times10^{-8}$)	X_{CH_3COOH} ($\times10^{-8}$)
G19.61−0.23[a].....	7.5	43.1	11.7	>3.7
G45.47+0.05[a].....	>0.01	>0.04	>0.007	>0.02
W75N[b].....	2.7	10.6	>0.5	>2.6

Note.—All upper limits were calculated from the 1 σ rms noise in the spectral window, the source sizes, and temperatures of 230, 81, and 242 K for G19.61−0.23, G45.47+0.05, and W75N, respectively (see §§ 4.2–4.3). For the upper limit of $HCOOCH_3$, we used a frequency of 111.453 GHz; for CH_3CH_2CN, 107.492 GHz; for HCOOH, 108.126 GHz; and for CH_3COOH, 111.549 GHz.

[a] H_2 column density taken from Fontani et al. (2002).

[b] H_2 column density taken from Zinchenko et al. (2000).

$HCOOCH_3$ and HCOOH is located ∼2.″7 to the east of the CH_3CN peak and has a cometary morphology similar to that seen by Liu et al. (2002) toward Orion. The CH_3CN emission, on the other hand, falls very close to the continuum emission, which is offset from the $HCOOCH_3$ and HCOOH emission. Indeed, the W75N region is more similar to the hot core regions surrounding W3 and Orion that show a differentiation between the O and N cores than to the W51e2 or Sgr B2(N-LMH) HMCs. Further high-resolution observations are necessary to investigate the O and N cores toward this region.

4.4. *Implications for Future Acetic Acid* (CH_3COOH) *Surveys*

Recalling the conclusions reached by Remijan et al. (2003) that CH_3COOH sources are HMCs located within 7 kpc of the Galactic center, have a mass range between 200 and 2000 $M_\odot$, and did not show a differentiation between O and N bearing cores, we discuss the validity of these criteria in light of the new nondetections. The distances and mass requirements are met as a result of source selection (except for W75N, which at a galactocentric distance of 8 kpc is outside the 7 kpc limit; however, given the mass and size of this source and the errors involved in distance determination, we believed W75N would be a good source to survey for CH_3COOH). We determined that G45.47+0.05 does not contain a hot compact core. The implication from the CH_3CN rotation diagram is that the molecular emission is extended and may contain several distinct sources. Because we believe CH_3COOH is formed in warm HMCs, we would not expect to detect it toward this region. We find that W75N has different O and N cores similar to W3(OH)/W3(H_2O) or the Orion Compact Ridge/Hot Core. With this discovery, we would not expect to detect CH_3COOH in this region. We can also rule out the O and N differentiation is due to our ability to resolve out the individual O and N cores in these sources. While it is true that each source in which O and N chemical differentiation has been seen is at a heliocentric distance of less than 3 kpc, we note that G19.61−0.23 does not show such a distinction at a heliocentric distance of 3.6 kpc. This leaves G19.61−0.23 as the lone remaining suitable CH_3COOH source. G19.61−0.23 seemed to fit all the selection criteria, and, in fact, there is an indication of an CH_3COOH transition at 111.507 GHz; however, the corresponding A transition at 111.549 GHz is not seen (Fig. 1). It appears that the chemistry present toward G19.61−0.23 is similar to G34.3+0.2. If you compare our Figure 3 and Figure 3 from Remijan et al. (2003), it is clear that all the same transitions of each molecular species are detected; however, the spectral lines toward G19.61−0.23 are all weaker by a factor of ∼2–3. If we apply the same reduction to the acetic acid lines, we find the acetic acid transitions should have a peak line intensity between 0.07 and 0.1 Jy beam^{-1}. The noise level in the acetic acid windows toward G19.61−0.23 was ∼0.05 Jy beam^{-1}, so we would only expect to detect these lines at the 1–2 σ level. Thus, to be confident in a detection, we would need to decrease the noise level to ∼0.02 Jy beam^{-1} for a 3–5 σ detection. We expect that further observations with a better signal-to-noise ratio should detect these lines. Therefore, in summary, our new results remain consistent with the conclusions of Remijan et al. (2003). Apparently, the formation of CH_3COOH favors HMCs with well-mixed N and O, despite the fact that CH_3COOH does not contain a N atom. If proved to be true, this is an important constraint on CH_3COOH formation and possibly other structurally similar biomolecules.

CH_3CN appears to be a good proxy in the search for hard-to-detect large molecular species, particularly in light of the potential importance of N chemistry. This is because CH_3CN is easily detectable and has a column density similar to the hard-to-detect large molecules (Remijan et al. 2003). Figure 10 illustrates this toward each of our SFRs, along with the previously observed sources Sgr B2(N-LMH) and W51e2 (Remijan et al. 2004, 2002; Snyder et al. 2002). In this case, each molecular species is plotted as a fractional abundance relative to CH_3CN. In nearly every case, we note that the CH_3CN column density is similar to the column densities of CH_3COOH, HCOOH, and CH_3CH_2CN. However, the measured relative abundances of $HCOOCH_3$ are often several times larger than those of any other molecular species. Thus, while CH_3CN appears to have a column density closer to that of the large molecular species, it is still not clear how CH_3CN is related to the chemistry that forms these large molecules, especially in those regions that have O- and N-rich cores. The only analysis trying to explain the formation of O- and N-rich cores was performed by Rodgers & Charnley (2001). They determined that the

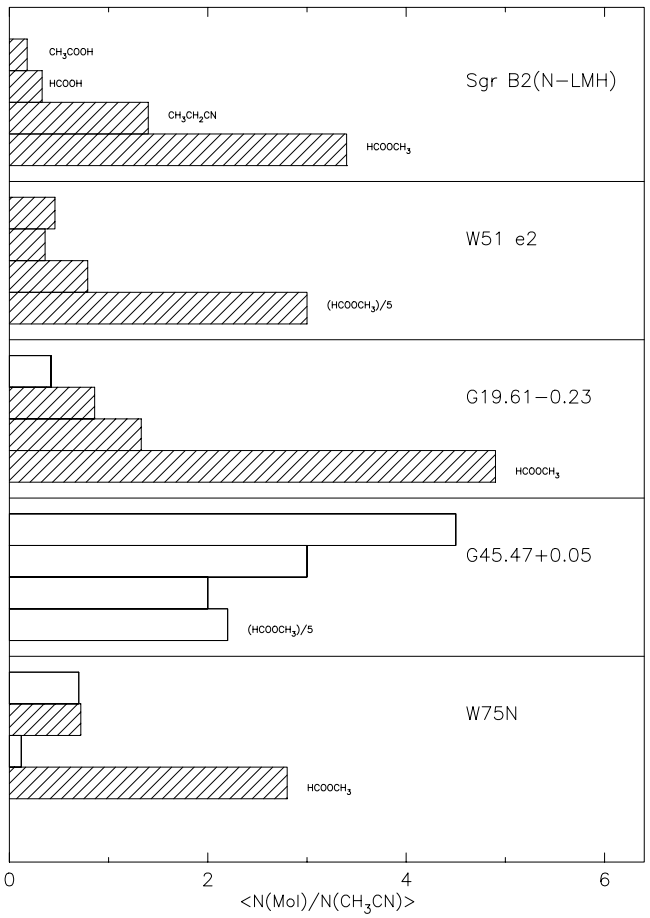

FIG. 10.—Beam-averaged fractional abundances relative to methyl cyanide (CH_3CN) for Sgr B2(N-LMH), W51e2, G19.61−0.23, G45.47+0.05, and W75N interferometric measurements. The hatching scheme is the same as in Fig. 9. The first bar corresponds to the fractional abundance of CH_3COOH, the second bar corresponds to the fractional abundance of HCOOH, the third bar corresponds to the fractional abundance of CH_3CH_2CN, and the fourth bar corresponds to the fractional abundance of $HCOOCH_3$ toward each source. Toward W51e2 and G45, note that the fractional abundance of $HCOOCH_3$ is divided by a factor of 5 for purposes of this display.

O- and N-rich cores are formed as a result of the abundance (or lack) of ammonia (NH_3) on grain mantles and the timescale of the core formation: O-rich cores form first, then they become N-rich. However, our observations indicate that large molecules are found in regions in which the formation of O- and N-rich cores is occurring simultaneously in the interstellar environment. Because CH_3CN lines are easy to detect, by first observing a source for CH_3CN, one can obtain information about the column densities of the larger molecules and, from that, an approximate line intensity. This will undoubtedly influence future surveys and at the same time help to gain an understanding of the physical conditions present toward future surveyed sources.

5. SUMMARY

We have surveyed three high-mass Galactic SFRs for interstellar methanol (CH_3OH), formic acid (HCOOH), acetic acid (CH_3COOH), methyl formate ($HCOOCH_3$), methyl cyanide (CH_3CN), and ethyl cyanide (CH_3CH_2CN) with the BIMA Array. From our observations, we have detected two new sources of interstellar HCOOH toward the hot core regions G19.61−0.23 and W75N. We have also made the first detections of CH_3CH_2CN and $HCOOCH_3$ toward G19.61−0.23. The relative $HCOOH/HCOOCH_3$ abundance ratio is 0.18, which is comparable to the abundance ratios found by Liu et al. (2001) toward Sgr B2(N-LMH), Orion, and W51 (∼0.10). We have made the first detection of $HCOOCH_3$ toward W75N. The relative $HCOOH/HCOOCH_3$ abundance ratio is 0.26, which is more than twice as large as the abundance ratios found by Liu et al. (2001). Furthermore, the hot core regions around W75N show for the first time a chemical differentiation between the O and N cores similar to that seen toward the Orion Hot Core and Compact Ridge and W3(OH) and W3(H_2O). It is also apparent from our observations that the high-mass SFR G45.47+0.05 does not contain any compact HMC, and its chemistry may be more similar to cold dark clouds. Finally, it appears that CH_3CN is a good tracer for harder to detect biomolecules. CH_3CN was detected toward all three sources, and, as Figures 9 and 10 illustrate, the total source-averaged CH_3CN column density is similar to the larger molecular species. Because CH_3CN lines appear easy to detect by first observing a source for CH_3CN, one can obtain information about the column densities of the larger biomolecules and, from that, an approximate line intensity. This will undoubtedly influence future surveys and at the same time help to gain an understanding of the physical conditions present toward future surveyed sources.

We are indebted to C. Watson for use of his BIMA data toward W75N. We thank F. J. Lovas for the use of his new line list of identified molecular species to identify spectral features in our passbands. We appreciate helpful comments from J. M. Hollis and E. C. Sutton. We thank an anonymous referee for some very useful comments. We acknowledge support from the Laboratory for Astronomical Imaging at the University of Illinois and NSF AST 99-81363 and AST 02-28953.

REFERENCES

Anderson, T., Crownover, R. L., Herbst, E., & de Lucia, F. C. 1988, ApJS, 67, 135
Boucher, D., Burie, J., Bauer, A., Dubrulle, A., & Demaison, J. 1980, J. Phys. Chem. Ref. Data, 9, 659
Churchwell, E., Walmsley, C. M., & Cesaroni, R. 1990, A&AS, 83, 119
Churchwell, E., Walmsley, C. M., & Wood, D. O. S. 1992, A&A, 253, 541
Comoretto, G., et al. 1990, A&AS, 84, 179
Fontani, F., Cesaroni, R., Caselli, P., & Olmi, L. 2002, A&A, 389, 603
Forster, J. R., & Caswell, J. L. 1989, A&A, 213, 339
Garay, G., Moran, J. M., Rodríguez, L. F., & Reid, M. J. 1998, ApJ, 492, 635
Garay, G., Reid, M. J., & Moran, J. M. 1985, ApJ, 289, 681
Gasiprong, N., Cohen, R. J., & Hutawarakorn, B. 2002, MNRAS, 336, 47
Gibb, E., Nummelin, A., Irvine, W. M., Whittet, D. C. B., & Bergman, P. 2000, ApJ, 545, 309
Goldsmith, P. F., & Langer, W. D. 1999, ApJ, 517, 209
Hatchell, J., Thompson, M. A., Millar, T. J., & MacDonald, G. H. 1998, A&AS, 133, 29
Helmich, F. P., Jansen, D. J., de Graauw, Th., Groesbeck, T. D., & van Dishoeck, E. F. 1994, A&A, 283, 626
Helmich, F. P., & van Dishoeck, E. F. 1997, A&AS, 124, 205
Hofner, P., & Churchwell, E. 1996, A&AS, 120, 283
Hofner, P., Wyrowski, F., Walmsley, C. M., & Churchwell, E. 2000, ApJ, 536, 393
Hollis, J. M., Vogel, S. N., Snyder, L. E., Jewell, P. R., & Lovas, F. J. 2001, ApJ, 554, L81
Hunter, T. R., Taylor, G. B., Felli, M., & Tofani, G. 1994, A&A, 284, 215
Ikeda, M., Ohishi, M., Nummelin, A., Dickens, J. E., Bergman, P., Hjalmarson, Å., & Irvine, W. M. 2001, ApJ, 560, 792
Ilyushin, V. V., et al. 2001, J. Mol. Spectrosc., 205, 286

Kalenskii, S. V., Berulis, I. I., Val'tts, I. E., Dzura, A. M., Slysh, V. I., & Vasil'kov, V. I. 1994, AZh, 71, 51
Kalenskii, S. V., Slysh, V. I., & Val'tts, I. E. 2002, Astron. Rep., 46, 96
Kurtz, S., Cesaroni, R., Churchwell, E., Hofner, P., & Walmsley, C. M. 2000, in Protostars and Planets IV, ed. V. Manning, A. P. Boss, & S. Russell (Tucson: Univ. Arizona Press), 299
Larionov, G. M., Val'tts, I. E., Winnberg, A., Johansson, L. E. B., Booth, R. S., & Golubev, V. V. 1999, A&AS, 139, 257
Lekht, E. E., & Krasnov, V. V. 2000, Astron. Lett., 26, 38
Lekht, E. E., Silant'ev, N. A., Mendoza-Torres, J. E., & Tolmachev, A. M. 2002, Astron. Lett., 28, 89
Liu, S.-Y., Girart, J. M., Remijan, A. J., & Snyder, L. E. 2002, ApJ, 576, 255
Liu, S.-Y., Mehringer, D. M., & Snyder, L. E. 2001, ApJ, 552, 654
Lovas, F. J. 1982, J. Phys. Chem. Ref. Data, 11, 251
Matthews, H. E., Goss, W. M., Winnberg, A., & Habing, H. J. 1977, A&A, 61, 261
Mehringer, D. M., Goss, W. M., & Palmer, P. 1995, ApJ, 452, 304
Minier, V., Conway, J. E., & Booth, R. S. 2001, A&A, 369, 278
Nummelin, A., Bergman, P., Hjalmarson, Å., Friberg, P., Irvine, W. M., Millar, T. J., Ohishi, M., & Saito, S. 2000, ApJS, 128, 213
Oesterling, L. C., Sieghard, A., de Lucia, F. C., Sastry, K. V. L. N., & Herbst, E. 1999, ApJ, 521, 255
Olmi, L., Cesaroni, R., & Walmsley, C. M. 1993, A&A, 276, 489
Palmer, P., Goss, W. M., & Devine, K. E. 2003, ApJ, 599, 324
Palmer, P., Goss, W. M., & Whiteoak, J. B. 2004, MNRAS, 347, 1164
Pankonin, V., Churchwell, E., Watson, C., & Bieging, J. H. 2001, ApJ, 558, 194
Remijan, A., Snyder, L. E., Friedel, D. N., Liu, S.-Y., & Shah, R.-Y. 2003, ApJ, 590, 314
Remijan, A., Snyder, L. E., Liu, S.-Y., Mehringer, D. M., & Kuan, Y.-J. 2002, ApJ, 576, 264
Remijan, A., Sutton, E. C., Snyder, L. E., Friedel, D. N., Liu, S.-Y., & Pei, C.-C. 2004, ApJ, 606, 917
Rodgers, S. D., & Charnley, S. B. 2001, ApJ, 546, 324
Sault, R. J., Teuben, P. J., & Wright, M. C. H. 1995, in ASP Conf. Ser. 77, Astronomical Data Analysis Software and Systems IV, ed. R. A. Shaw, H. E. Payne, & J. J. E. Hayes (San Francisco: ASP), 433
Shirley, Y. L., Evans, N. J., Young, K. E., Knez, C., & Jaffe, D. T. 2003, ApJS, 149, 375
Snyder, L. E., Lovas, F. J., Mehringer, D. M., Miao, Y., Kuan, Y.-J., Hollis, J. M., & Jewell, P. R. 2002, ApJ, 578, 245
Torelles, J. M., Gomez, J. F., Rodríguez, L. F., & Ho, P. T. P. 1997, ApJ, 489, 744
Valdetto, R., Palla, F., Brand, J., Cesaroni, R., Comoretto, G., & Felli, M. 2002, A&A, 383, 244
Voronkov, M. A., Austin, M. C., & Sobolev, A. M. 2002, A&A, 387, 310
Watson, C., Churchwell, E., Pankonin, V., & Bieging, J. H. 2002, ApJ, 577, 260
Westerhout, G. 1958, Bull. Astron. Inst. Netherlands, 14, 215
Willemot, E., Dangoisse, D., Monnanteuil, N., & Bellet, J. 1980, J. Phys. Chem. Ref. Data, 9, 59
Wu, J., & Evans, N. J. 2003, ApJ, 592, L79
Xu, L. H., & Lovas, F. J. 1997, J. Phys. Chem. Ref. Data, 26, 17
Zheng, X.-W., & Ling, Z.-F. 1997, Acta Astron. Sinica, 38, 135
Zinchenko, I., Henkel, C., & Mao, R. Q. 2000, A&A, 361, 1079